Micro-electromechanical System Sensors in Unscented Kalman Filter-based Condition Monitoring of Hydraulic Systems

Jarmo Nurmi, Janne Honkakorpi, Juho Vihonen, and Jouni Mattila

***Abstract*—A condition monitoring system of mechatronic design using an easy-to-install micro-electromechanical system-based (MEMS) motion sensor is developed in this paper, since the joint encoders and resolvers that require mechanical joint modifications are not often a realistic option for mobile machines. This paper presents an unscented Kalman filter-based (UKF) condition monitoring scheme for leakage detection in hydraulic actuator systems using the joint sensor feedback. By comparing the UKF residuals of the developed MEMS sensor to the residuals of a highly accurate reference encoder, we show that the developed easy-to-install and low-cost MEMS sensor is suitable for this condition monitoring task.**

I. Introduction

Hydraulically driven heavy-duty manipulators and cranes are widely used e.g. in material and cargo handling, construction and mining industries. These systems are still predominantly open-loop controlled by human operators and thus do not have any joint sensor instrumentation. However, the manufacturers of these machines have great interest to increase their after-sales market offering in particular in condition monitoring and machine operation optimization. Introducing advanced software-based functionality such as condition monitoring still requires motion sensors that would to be easily retrofitted into these machines. The traditional option for retrofitting would be joint angle encoders or resolvers, but these sensors are often of high-cost (> 300 €), not suitable for rugged environments and their installation requires modifications prone to mechanical failures. Therefore, we foresee that easy to retrofit, low-cost (~ 100€ mass-produced) MEMS sensor technology embedded with advanced signal processing is required to enable the conditions monitoring applications.

Previous work in the development of MEMS sensor technology includes e.g. [1], [2], [3] where measurements from multiple accelerometers were combined, and [4] where low-cost tilt sensor, rate gyro and accelerometer measurements were fused. In terms of condition monitoring, the use of similar MEMS sensor measurements has been limited to vibration analysis, see e.g. [5], [6]. In this paper, a different approach to condition monitoring is taken by considering the utilization of the developed MEMS motion sensor in a model-based load-independent condition monitoring algorithm for a hydraulic manipulator where from the two-fold mechatronic perspective, firstly the algorithm development for the robust, low-cost and easy-to-install embedded motion sensor prototype is presented, and secondly its application to condition monitoring is demonstrated. The algorithm is founded on the principle of complementary filtering to improve the quality of position and velocity measurements. The condition monitoring capability is demonstrated by comparison with a high accuracy reference sensor (joint angle encoder) in a generic and easily parametrisable scheme for a hydraulic application where for example a joint angle encoder is not a realistic design option to satisfy the requirements of easy installation and retrofitting to existing machines. The MEMS sensor on the other hand satisfies these requirements and is thus a suitable candidate to enable advanced functionality such as condition monitoring.

In reference to prior work by the authors, contrary to [7], the easily applicable MEMS-based sensor is here used in place of the unrealistic option, the joint angle encoder in unscented Kalman filter-based (UKF) fault detection. The UKF fault detection is based on the residual between the system model and measurement. Implementation of the load-independent UKF condition monitoring system with the MEMS sensor is novel in reference to prior work. Additionally, previously in [8] the successful application of the MEMS sensor to hydraulic manipulator state feedback control was shown, and so this paper expands the possible application range of the MEMS sensor to make it more attractive to mobile machine manufacturers looking to compete in the global market with novel functionalities and services.

This paper is organized as follows. In Section II, sensors in hydraulic manipulator control are discussed with a focus on the developed MEMS sensor prototype and its algorithms. The UKF and the reduced-order model of a servo valve-controlled hydraulic cylinder are introduced in Section III. In Section IV, the performance of the MEMS sensor is experimentally assessed and compared against encoder measurements. Section V discusses the obtained results. Finally, the conclusions are drawn in Section VI. The paper concludes with an appendix containing the UKF algorithm.

II. Sensors in hydraulic control

In hydraulic control applications, the design of a high-quality controller is of great importance in achieving desirable properties, such as accurate tracking and minimization of positioning errors. Regardless of controller design, these properties cannot be achieved without a high-

This work was supported in part by the Academy of Finland under project 133273.

Jarmo Nurmi and Janne Honkakorpi are researchers at the Dept. of Intelligent Hydraulics and Automation, Tampere University of Technology, e-mails: jarmo.nurmi@tut.fi, janne.honkakorpi@tut.fi.

Juho Vihonen is a post-doctoral researcher at the Dept. of Signal Processing, Tampere University of Technology, e-mail: juho.vihonen@tut.fi

Jouni Mattila is a professor of machine automation at the Dept. of Intelligent Hydraulics and Automation, Tampere University of Technology, e-mail: jouni.mattila@tut.fi.

quality measurement of the joint angle. Most often the joint angle is measured with a rotary resolver or encoder due to their accuracy. However, they are usually expensive and cannot be easily retrofitted to existing machines because of the requirement of contact to the joint axle or a shaft between adjacent links if the axle is non-rotary (Fig. 1). The installation of the encoder also requires high co-axial precision and if the installation is done poorly, the accuracy and mechanical durability of the sensor could be compromised.

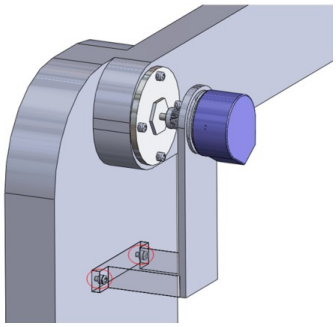

Figure 1. Installation of an angle encoder to the joint of a manipulator.

To overcome these limitations of the resolvers and encoders, the Department of Intelligent Hydraulics and Automation of Tampere University of Technology has developed a MEMS sensor module suitable for the harsh working conditions of mobile working machines where the MEMS chip integrates micromechanical structures and some signal conditioning electronics onto a single silicon chip. The mechanism sizes are minute and hence well-suited to cramped spaces with requirements of high chip-level integration. The module is encased in an epoxy-filled dust- and waterproof aluminium enclosure as shown in Fig. 2. The MEMS chip is the model SCC1300-D02 by Murata Electronics, which combines a three-axis accelerometer with a one-axis rate gyroscope.

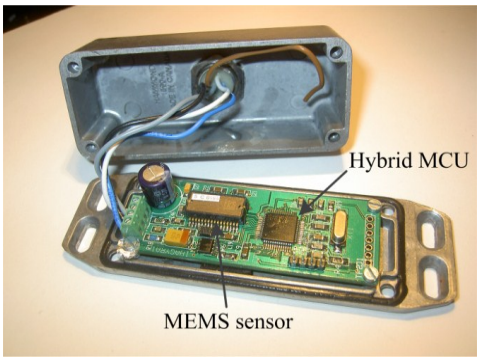

Figure 2. The developed MEMS sensor prototype (without epoxy filling).

The accelerometer measures linear acceleration along the three axes and can also measure inclination angles with the application of inverse trigonometric functions to observed vector components of gravitational acceleration. The digital output of the accelerometer has a resolution of 0.56 mg per least significant bit (LSB) which translates into a best-case inclination resolution of 0.032 deg when the accelerometer axis is parallel to ground. However, if the accelerometer is placed far away from the axis of rotation, the gravity sensing can be impaired. The digital signal of the gyro has a resolution of 0.02 deg/s per LSB. The MEMS chip has been combined with a 16-bit hybrid signal microcontroller unit (MCU) and a line driver chip for implementing low-level data operations and CANopen communication. This makes the sensor module well suited for retrofit-type integration into existing platforms.

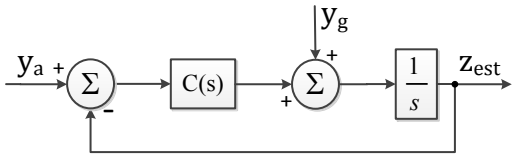

Figure 3. Complementary filter structure.

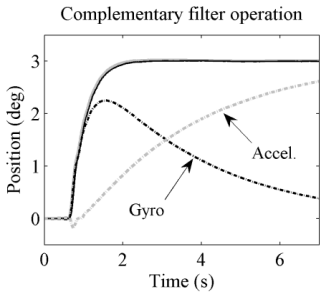

Figure 4. Example complementary filter output (solid black line) versus encoder position (solid grey line) when given a step input.

As stated previously, a recently developed approach to measure inclination angles with MEMS sensors has been the use of more than one accelerometer to measure the same joint angle [1], [2], [3]. Kalman filtering has also been applied when fusing accelerometer and gyroscope measurements [9], [10]. The developed MEMS sensor prototype, on the other hand, uses complementary filtering [8], [11] to produce angular values by fusing the advantageous static performance of the accelerometer with the favourable dynamic performance of the gyroscope. The accelerometer inclination angle and gyro rate output are governed by

$$y_a = z + \eta_a \quad (1)$$

$$y_g = dz/dt + \eta_g + b \quad (2)$$

where z is the actual inclination angle, η_a is the accelerometer output noise, η_g is the gyro output noise which is predominantly of high frequency like the accelerometer noise term but typically has less variance, and b is a bias term which is predominantly low frequency disturbance.

The complementary filter is implemented with a linear feedback system as shown in Fig. 3 where the combined output of the accelerometer inclination angle y_a and the gyro angular velocity output y_g has the Laplace representation

$$z_{est} = [C(s)y_a]/[s + C(s)] + [y_g s]/[s^2 + C(s)s] \quad (3)$$

where C(s) can be chosen as the PI-controller, i.e. $C(s) = K_P + K_I/s$ so that $G(s) = C(s)/[s+C(s)]$ is a low-pass filter, and its complement $1 - G(s) = s/[s+C(s)]$ is a high-pass filter. In the

PI-controller case, the time domain dynamics are governed by

$$dz_{est}/dt = y_g - b_i + K_P(y_a - z_{est}) \quad (4)$$

$$db_i/dt = -K_I(y_a - z_{est}) \quad (5)$$

where K_P defines the crossover frequency chosen as a trade-off based on the low-pass characteristics of the accelerometer-based inclination and the low frequency bias characteristics of the gyroscope rate measurements. A non-zero K_I rejects a load disturbance b_i from the output.

The time domain operation of the complementary filter is illustrated in Fig. 4, where the initial dominance of the gyro followed by its slowly decaying effect, and conversely, the minor initial effect of the accelerometer followed by steady-state dominance show clearly. The resultant output has a typical steady-state error within ±0.05 degrees whereas the dynamic error is directly proportional to movement velocity. The high accuracy reference sensor output shown in solid grey color was from a Heidenhain incremental encoder with a resolution of 0.00075 degrees per pulse.

III. Condition Monitoring with Unscented Kalman Filter Using MEMS Sensor

Model-based fault detection and isolation (FDI) with UKF was shown in [7], [12] by the authors in a proportional valve controlled 1-DOF hydraulic application in which leakages were emulated and valve faults were simulated under varying load. Now we consider using the developed robust, low-cost MEMS sensor in place of the high accuracy reference sensor in the same application for measuring joint angle and angular velocity. In this section, the procedure for applying the UKF to FDI is described, but it is to be noted that the paper focuses mainly on comparing fault detection capabilities of the different sensors by residual analysis.

A. Principle of unscented Kalman filter-based condition monitoring

Condition monitoring with the UKF is an observer-based method belonging to the class of model-based methods. The model-based condition monitoring is established around the concept of analytical redundancy which originates from running the plant model in parallel to the real physical system, see Fig. 5. The scheme is to subtract plant model output $\hat{y}(k)$ (in this case an UKF estimate) from actual measurement $y(k)$ to create a residual $r(k)$ that reveals the system condition [13]. The residual should be close to zero in faultless operation, assuming that measurement noise is minor and the plant model is accurate. After the appearance of a fault, if the residual is sensitive to the fault, the residual differs from zero thus enabling fault detection. Following fault detection, the cause of the fault is isolated by examining the residual for known patterns. For example in hydraulic systems, external leakages are known to mainly affect the pressure residual of cylinder chamber A or B depending on whether the leakage is on the A or B side, whereas internal leakages affect both the A and B pressure residuals.

The benefits of using UKF in the FDI of hydraulic systems are increased robustness towards process and measurement noise, and the suitability for nonlinear systems if compared with linear FDI filters. It is suitable for general problems with nonlinear process and measurement models

$$\mathbf{x}_{k+1} = \mathbf{f}(\mathbf{x}_k, \mathbf{u}_k) + \mathbf{w}_k \quad (6)$$

$$\mathbf{y}_{k+1} = \mathbf{h}(\mathbf{x}_{k+1}) + \mathbf{v}_{k+1} \quad (7)$$

where $\boldsymbol{x}_{k+1}$ is a state vector, $\boldsymbol{f}(\ldots)$ is the process model, $\boldsymbol{u}_k$ is a control vector, $\boldsymbol{w}_k$ is a process noise vector, $\boldsymbol{y}_{k+1}$ is a measurement vector, $\boldsymbol{h}(\ldots)$ is the measurement model, $\boldsymbol{v}_{k+1}$ is a measurement noise vector, and k is a discrete time step.

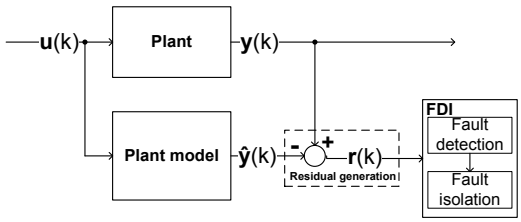

Figure 5. Principle of model-based condition monitoring [13].

The increased robustness of the UKF leads to a non-drifting state estimate in case of bounded short term modeling errors or measurement noise. The nonlinearity property of the UKF allows the modeling of the inherent nonlinearities of hydraulic systems, such as actuator friction, and valve properties including turbulent flow, dead zone, hysteresis, saturation and nonlinear opening. When estimating the states of the above system, the UKF is also typically more efficient than for example a particle filter, which requires the re-sampling of numerous particles at the cost of computational complexity.

To gain efficiency, the UKF carries out an unscented transformation (UT), a technique using deterministic sampling for estimating the mean and covariance of states after they have been transformed through nonlinear equations. The UKF thus avoids the linearization which is partly responsible for estimation errors for example in many extended Kalman filter (EKF) applications. The use of UKF over EKF is further justified by its usually increased accuracy in estimating the true mean and covariance of states [14], [15]. The UKF algorithm is summarized in the Appendix.

B. Reduced-order model of a proportional valve controlled hydraulic cylinder

The reduced state vector of the hydraulic system consisting of a fast proportional valve controlling a hydraulic cylinder is

$$\boldsymbol{x} = [p_A, p_B, x_s, dx_s/dt]^T \quad (8)$$

where p_A is the pressure in cylinder chamber A (piston-side), p_B is the pressure in cylinder chamber B (rod-side), x_s is the spool position of the valve, and dx_s/dt is the spool velocity.

The control vector of the system is:

$$\boldsymbol{u} = [x, dx/dt, u_v, p_s]^T \quad (9)$$

where x and dx/dt are the piston position and velocity, u_v is valve control signal, and p_s is the supply pressure. Note that the piston position and velocity can be obtained via geometrical transformations from the joint angle and angular velocity measurements.

The continuous-time dynamics for the system are

$$\begin{aligned}
\dot{x}_1 &= f_1(x_k,u_k) = \frac{B_{effA}}{V_{0A}+A_A u_1}\left(Q_A - A_A u_2\right)\\
\dot{x}_2 &= f_2(x_k,u_k) = \frac{B_{effB}}{V_{0B}+A_B(x_{\max}-u_1)}\left(Q_B + A_B u_2\right)\\
\dot{x}_3 &= f_3(x_k,u_k) = x_4\\
\dot{x}_4 &= f_4(x_k,u_k) = K\omega_n u_3 - 2\omega_n d_r x_4 - \omega_n^2 x_3
\end{aligned} \tag{10}$$

where B_{effX} is the effective bulk modulus in chamber X, V_{0X} is the chamber volume X, A_X is the cross-sectional cylinder area in chamber X, Q_X is the flow to and from chamber X, for $X = \{A, B\}$, x_{max} is the cylinder stroke, K is the gain from valve control signal to spool position, ω_n is the natural frequency of the spool, and d_r is the damping ratio. Note that the piston position and velocity are treated as inputs as described by (9). Thus the piston dynamics can be excluded from the system model described by (10), which guarantees independence from load force and mass.

The flow rates Q_A and Q_B from (10) are as follows

$$Q_A = \begin{cases}
K_{vPA}x_s\sqrt{|p_s - p_A|}\,\mathrm{sgn}(p_s - p_A), x_s \geq 0.01\\
K_{vAT}x_s\sqrt{|p_A - p_T|}\,\mathrm{sgn}(p_s - p_A), x_s \leq -0.01\\
K_{vPAleak}(p_s - p_A)\\
-K_{vATleak}(p_A - p_T), |x_s| < 0.01
\end{cases} \tag{11}$$

$$Q_B = \begin{cases}
-K_{vBT}x_s\sqrt{|p_B - p_T|}\,\mathrm{sgn}(p_B - p_T),\\
x_s \geq 0.01\\
-K_{vPB}x_s\sqrt{|p_S - p_B|}\,\mathrm{sgn}(p_s - p_B),\\
x_s \leq -0.01\\
K_{vPBleak}(p_s - p_B)\\
-K_{vBTleak}(p_B - p_T), |x_s| < 0.01
\end{cases} \tag{12}$$

where p_T is the tank pressure, K_{vX} and $K_{vX,leak}$ are the flow coefficient and leakage flow coefficient, respectively, of notch X, for $X = \{PA, AT, BT, PB\}$.

By discretizing (10) with Euler's forward method, the states are transferred a time step forward with

$$x_{n,k+1} = x_{n,k} + f_n(\boldsymbol{x}_k, \boldsymbol{u}_k)\Delta T \tag{13}$$

where n = 1,2,...,4, k is the time index, and ΔT is the fixed time step. As explained in [7], there was a linear relation between states and measurements:

$$\hat{\mathbf{y}}_{k+1}^{-} = \begin{bmatrix} 1 & 0 & 0 & 0 \\ 0 & 1 & 0 & 0 \end{bmatrix} \hat{\mathbf{x}}_{k+1}^{-} \tag{14}$$

IV. Experiments

A. Test bed and measurements

Using the model presented in Section III.B, the UKF is designed for a 1-DOF hydraulic test bed shown in Fig. 6. The load masses of the system are set to 494 kg on the left, zero on the right, and additionally, the boom weighs 297 kg.

Shown in the hydraulic diagram in Fig. 7, the proportional 4/3-directional valve (24 L/min @ 3.5 MPa) controls the flow to the asymmetrical cylinder (Ø80/45-545). The restrictor valves (labeled 'Internal leakage', 'External leakage A' and 'External leakage B') are needle valves (30 L/min @ 40 MPa) which emulate leakage faults that often in reality require halting system operation after FDI to minimize damage to the environment. The cylinder chamber and the supply pressures are measured with pressure transmitters having a 0-25 MPa operating range. The control signal of the valve is also measured, as are the boom joint angle θ and boom joint angular velocity dθ/dt that are measured with the reference sensor (Heidenhain encoder), and the discussed MEMS sensor prototype that is installed near the rotating joint of the test bed to avoid any perturbations in the accelerometer readings due to centrifugal forces.

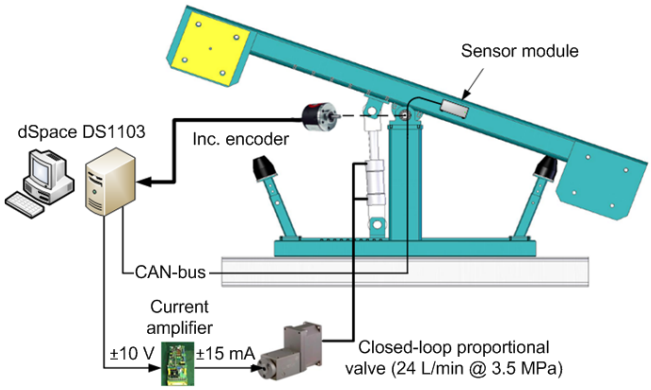

Figure 6. Illustration of test bed setup.

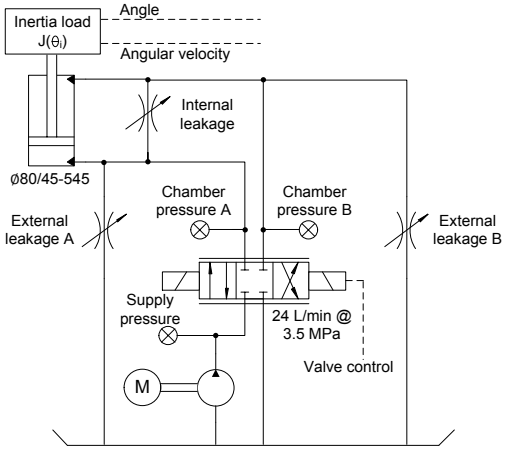

Figure 7. Hydraulic diagram of test bed.

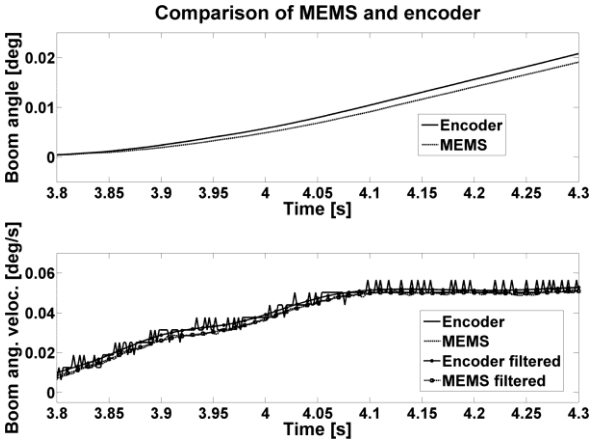

Figure 8. Angle and angular velocity measurements from the angle encoder (solid), MEMS sensor (dashed), filtered encoder angular velocity (asterisk), and filtered MEMS sensor angular velocity (square).

A comparison of the encoder and MEMS measurements in a 0.50-second-window (Fig. 8) shows the performance difference between the sensors. One can see a steady-state error in the MEMS angle measurement and noise in the differentiated angular velocity of the encoder. The angle and angular velocity measurements from both sensors were converted to piston position and velocity and were then used as inputs to the UKF.

B. *Experimental comparison of MEMS and high accuracy encoder in condition monitoring*

A random user-input to the proportional valve was used in all fault-free and fault experiments while the boom angle was measured with both the MEMS sensor and encoder to facilitate a direct comparison between the sensor performances in this condition monitoring task. The performances of the MEMS sensor and angle encoder were compared in terms of pressure residual behavior by using the both sensor outputs as control inputs to the UKF. The residuals were calculated with

$$r_k = p_k - p_{est,k} \tag{15}$$

where p_k is the measured and $p_{est,k}$ the UKF estimated cylinder chamber pressure at time instant k. Pressure residuals were chosen over velocity and position residuals on the basis of their high sensitivity to leakages in the so-called global sensitivity analysis and to enable the important property of load independence; see [12]. The residuals were averaged within a moving window of 5 seconds, and they were paired with adaptive, pressure-dependent thresholds that were required to be crossed to induce an alarm to increase robustness against false alarms; see also [7]. The positive thresholds for the encoder and MEMS sensor systems, respectively, were experimentally set as follows

$$t_{pos,E}(\mu_{p,k}) = 0.015 + 4*10^{-4}\mu^2_{p,k} \tag{16}$$

$$t_{pos,M}(\mu_{p,k}) = 0.023 + 4*10^{-4}\mu^2_{p,k} \tag{17}$$

where μ_p is the cylinder chamber pressure averaged over a 5-second window. On the basis of experimental verification and fault-free experiments conducted in the next section, the first term of the MEMS threshold was set 53 percent higher than the first term of the encoder threshold to minimize false alarms. The process noise variances of the UKF in the MEMS system could have also been increased but that was not considered to allow a fair comparison between the sensors. The negative thresholds were derived from (15) and (16) by simple multiplication with minus one. Note that while this monitoring strategy based on moving average is suboptimum from the viewpoint of minimizing the delay for detection for a fixed mean time between false alarms, see e.g. [16], it allows simple comparison of the different sensors.

C. *Fault-free experiments*

In fault-free experiments, the residuals should stay within the thresholds, and preferably near zero to enable reliable condition monitoring. The premise is that the residual of the MEMS sensor is larger than that of the encoder due to the limited accuracy of the MEMS sensor. To verify this, a total of six fault-free experiments were used, one of which is shown in Fig. 9. From the figure, it can be seen that absolute values of the MEMS residuals are larger than encoder residuals, which lead to the higher threshold requirement for the MEMS sensor system discussed previously. For a numerical comparison between the different sensors, Table I shows the mean of the RMS' of the residuals calculated over the six fault-free experiments of varying durations from approximately 20 to 70 seconds and weighed in proportion to these durations. The results show that on average the MEMS pressure A residuals were 6 % and the pressure B residuals 59 % higher than encoder residuals. This implies poorer fault detection capability for the MEMS sensor system compared to the more accurate encoder system.

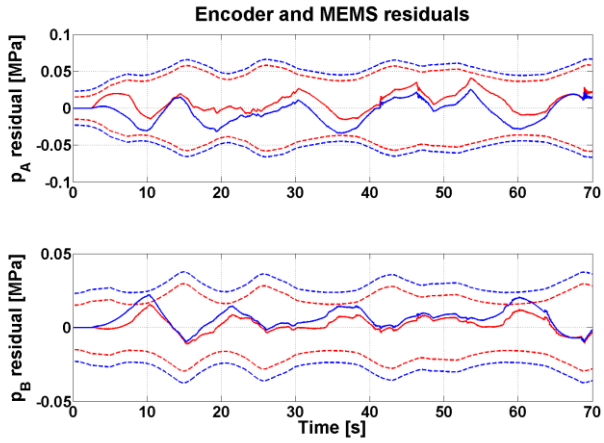

Figure 9. Pressure residuals with the encoder (red) and the MEMS sensor (blue) measurements in a fault-free experiment, the encoder thresholds in dashed red, MEMS thresholds in dashed blue.

TABLE I. RMS' CALCULATED FROM MEMS AND ENCODER MEASUREMENTS IN FAULT-FREE EXPERIMENTS

Sensor	Residual	RMS [MPa]
Encoder	p_A	0.0141
	p_B	0.0051
MEMS	p_A	0.0150
	p_B	0.0081

D. Fault case 1: External leakage in cylinder chamber B

Differences in fault detection capability between the encoder and MEMS sensor systems were studied with external leakage fault cases. An external leakage in cylinder chamber B (rod-side) was added to the system at the 26th second, shown in Fig. 10 with the solid vertical line, by opening the corresponding needle valve. After the introduction, the leakage magnitude was time-variant, see Section IV.F. The fault detection took over ten seconds with both the MEMS sensor and encoder since the residuals were forced to zero when the cylinder was completely retracted due to significant estimation errors in this situation. Overall, the MEMS sensor system was 6 seconds slower than the encoder system in fault detection, and at the time of detection the external leakage was approximately 0.2 L/min and 1.05 L/min with the encoder and the MEMS, respectively. The difference seems remarkable, but in reality the 0.2 L/min was 5.5 % of the flow passing through the proportional valve and the 1.05 L/min was 11 %.

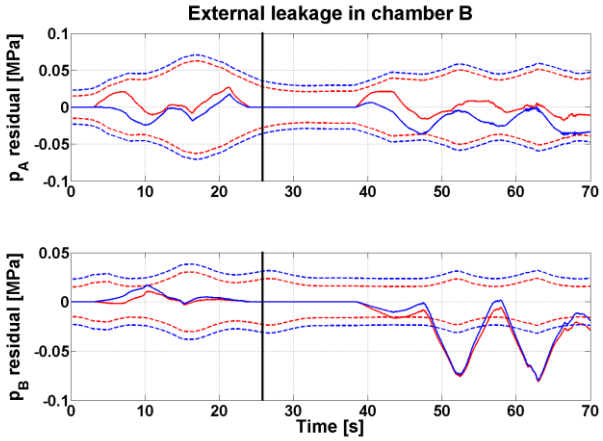

Figure 10. Pressure residuals with the encoder (red) and the MEMS sensor (blue) measurements when there is an external leakage in chamber B (rod-side), the encoder thresholds in dashed red, MEMS thresholds in dashed blue.

E. Fault case 2: Internal leakage in cylinder

Differences in fault detection capability between the encoder and MEMS sensor systems were also studied with internal leakage fault cases. An emulated internal leakage between cylinder chambers that was added to the system around the 30th second is shown in Fig. 11. The fault was detected approximately only 0.3 seconds sooner with the encoder than with the MEMS sensor. At the time of detection the leakage was 1.6 L/min and 1.5 L/min with the encoder and MEMS sensor, respectively. Of the flow through the proportional valve, the leakages were 21 % with the encoder and 19.5 % with the MEMS. Although the MEMS sensor system recognized a lower leakage, it performed worse by failing to recognize the previous 1.6 L/min leakage that was recognized successfully by the encoder system. The recognition of the lower leakage by the MEMS system was due to the delayed fault detection caused by the higher thresholds of the MEMS system, and the time-varying leakage to be discussed in Section IV.F.

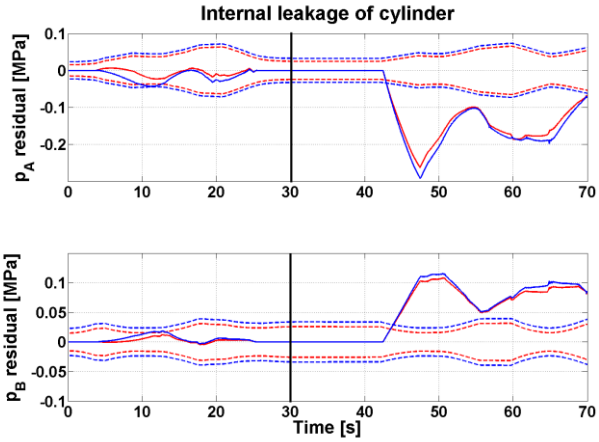

Figure 11. Pressure residuals with the encoder (red) and the MEMS sensor (blue) measurements when there is an internal leakage between cylinder chambers, the encoder thresholds in dashed red, MEMS thresholds in dashed blue.

F. Summary of fault experiments

In Sections IV.D and IV.E, the fault detection performance of the encoder and MEMS sensor were compared with the fault detection delay and with the proportion of the leakage flow rate to the total flow rate through the proportional valve at the time of detection. The MEMS sensor had generally higher fault detection delays than the encoder mainly due to its mandatory higher threshold selection based on the higher residual RMS' in fault-free experiments. The fault detection delay of the MEMS sensor was also greater in the external leakage experiment than in the internal leakage experiment because the internal leakage was generally of higher amplitude and thus resulted in higher absolute values of residuals with both sensor systems. Namely, the external leakage flow rate was 0.38±0.33 L/min with a maximum value of 1.52 L/min and a minimum of 0.04 L/min, whereas the internal leakage flow rate was 0.91±0.44 L/min with a single maximum of 6.49 L/min due to high-amplitude pressure oscillation and a minimum of 0.05 L/min. The proportions of the leak flow rates to the flow rates through the proportional valve at the fault detection instant were comparable between the two sensor systems.

TABLE II. RMS' CALCULATED FROM MEMS AND ENCODER MEASUREMENTS IN FAULT EXPERIMENTS.

Sensor	Fault	Residual	RMS [MPa]
Encoder	External leakage B	p_A	0.0119
		p_B	0.0388
Encoder	Internal leakage	p_A	0.1392
		p_B	0.0817
MEMS	External leakage B	p_A	0.0223
		p_B	0.0365
MEMS	Internal leakage	p_A	0.1534
		p_B	0.0868

To further compare the different sensors, RMS' of the residuals were calculated in fault experiments in a similar fashion as for Table I. These RMS' in Table II show that the operation of the encoder and MEMS sensor systems are

highly comparable in the internal leakage fault cases, but that the encoder performs better in the external leakage fault case by showing a smaller change in the p_A residual than the MEMS sensor, whereas p_B residual increases similarly with both sensor systems. Overall, the RMS' of the different sensors are reasonably well comparable and if compared with the Table I, they provide discriminability of sufficient degree. That is, the MEMS sensor system is capable of functioning in a condition monitoring system when the leakages are fairly minor, though the lowest detectable leakage was not sought here. If further considering the changes in the observed residuals and their signs in the Figs. 10 and 11 when a threshold is exceeded, monitoring the different combinations would allow one to conduct FDI for specifying the origin of the fault.

V. Discussion

The experimental results in the condition monitoring task of detecting oil leakages reveal the limited accuracy of the MEMS-based sensor when compared with the high-accuracy reference, the encoder, but the differences between the two sensor systems are not as drastic as what might be expected based on for example steady-state characteristics. A comparison of steady-state accuracies namely suggests that the encoder is ideally almost 67 times more accurate than the MEMS-based sensor with their accuracies 0.00075 ° and about 0.05 ° empirically found in [8], respectively. But in the condition monitoring, we found that fault detection was 0.3 to 6 seconds slower with the MEMS when the emulated oil leakages were between 0.2 to 1.6 L/min, RMS' of pressure residuals were 6 to 59 percent higher with MEMS sensor than with the encoder in fault-free experiments, and the RMS' in fault experiments were comparable to those. These figures do not resemble the remarkable difference in the estimated steady-state accuracies, which says that the limited accuracy of the MEMS sensor in the form of minor delay and bias does not cause modeling errors that would render it unsuitable for the condition monitoring task. In general, the MEMS measurement is corrupted by multiple error sources with complex mutual dependencies where, for example, scale factor and misalignment contributions depend on the boom dynamics. As the results show, the practical challenge related to the modeling of such error sources can be successfully overcome by the appropriate PI-type complementary filter, UKF covariance parameters, and the pressure residual threshold selection. Thus the MEMS may be considered as a cost-efficient, accurate enough tool for 1-DOF condition monitoring applications.

VI. Conclusion

In this paper, from the two-fold mechatronic perspective, firstly the accuracy and algorithms of the developed MEMS-based motion sensor prototype were presented and discussed. Secondly, the MEMS sensor was applied to an UKF-based condition monitoring scenario of a joint driven by a hydraulic cylinder. In that scenario, angle and angular velocity measurements provided by the developed MEMS sensor prototype and a high-accuracy reference sensor (joint angle encoder) were fed to the UKF as control inputs. Pressure residuals were then generated using both sensors and compared against each other in terms of behavior in fault-free and external and internal leakage experiments to study their effect on fault detection capability. Overall, the performance of the MEMS sensor was suitable for the condition monitoring task in this open-loop system and cannot be considered to be a more limiting factor than modeling errors. Hence the MEMS sensor is able to replace the expensive reference sensor in the model-based condition monitoring of 1-DOF open loop systems. In a closed-loop system though, where the effect of a fault must be compensated by reconfiguring the controller, the prolonged fault detection might have severe consequences.

Appendix

The equations of the unscented Kalman filter algorithm are [15]:

$$\begin{aligned}
&\hat{\mathbf{x}}_0 = \mathrm{E}(\mathbf{x}_0) \\
&\mathbf{P}_0 = \mathrm{E}\left[(\mathbf{x}_0 - \hat{\mathbf{x}}_0)(\mathbf{x}_0 - \hat{\mathbf{x}}_0)^{\mathrm{T}}\right] \\
&k = 0
\end{aligned} \tag{18}$$

$$\begin{aligned}
&\hat{\mathbf{x}}_k^{(0)} = \hat{\mathbf{x}}_k \\
&\hat{\mathbf{x}}_k^{(i)} = \hat{\mathbf{x}}_k + \tilde{\mathbf{x}}^{(i)}, i = 1,2,\ldots,2N \\
&\tilde{\mathbf{x}}^{(i)} = \sqrt{(N+\lambda)\mathbf{P}_k}^{\mathrm{T}}_i, i = 1,2,\ldots,N \\
&\tilde{\mathbf{x}}^{(i)} = -\sqrt{(N+\lambda)\mathbf{P}_k}^{\mathrm{T}}_i, i = N+1, N+2,\ldots,2N
\end{aligned} \tag{19}$$

$$\hat{\mathbf{x}}_{k+1}^{(i)} = \mathbf{f}(\hat{\mathbf{x}}_k^{(i)}, \mathbf{u}_k) \tag{20}$$

$$\begin{aligned}
&w_{mean}^{(0)} = \frac{\lambda}{N+\lambda} \\
&w_{mean}^{(i)} = \frac{1}{2(N+\lambda)}, i = 1,2,\ldots,2N \\
&\hat{\mathbf{x}}_{k+1}^{-} = \sum_{i=0}^{2N} w_{mean}^{(i)} \hat{\mathbf{x}}_{k+1}^{(i)}
\end{aligned} \tag{21}$$

$$\begin{aligned}
&w_{\mathrm{cov}}^{(0)} = \frac{\lambda}{N+\lambda} + (1 - \alpha^2 + \beta) \\
&w_{\mathrm{cov}}^{(i)} = \frac{1}{2(N+\lambda)}, i = 1,2,\ldots,2N \\
&\mathbf{P}_{k+1}^{-} = \sum_{i=0}^{i=2N} w_{\mathrm{cov}}^{(i)} (\hat{\mathbf{x}}_{k+1}^{(i)} - \hat{\mathbf{x}}_{k+1}^{-})(\hat{\mathbf{x}}_{k+1}^{(i)} - \hat{\mathbf{x}}_{k+1}^{-})^{\mathrm{T}} + \mathbf{Q}_k
\end{aligned} \tag{22}$$

$$\begin{aligned}
&\hat{\mathbf{y}}_{k+1}^{(i)} = \mathbf{h}(\hat{\mathbf{x}}_{k+1}^{(i)}, \mathbf{u}_k) \\
&\hat{\mathbf{y}}_{k+1} = \sum_{i=0}^{2N} w_{mean}^{(i)} \hat{\mathbf{y}}_{k+1}^{(i)} \\
&\mathbf{P}_{yy} = \sum_{i=0}^{2N} w_{\mathrm{cov}}^{(i)} (\hat{\mathbf{y}}_{k+1}^{(i)} - \hat{\mathbf{y}}_{k+1})(\hat{\mathbf{y}}_{k+1}^{(i)} - \hat{\mathbf{y}}_{k+1})^{\mathrm{T}} + \mathbf{R}_{k+1}
\end{aligned} \tag{23}$$

$$\mathbf{P}_{xy} = \sum_{i=0}^{2N} w_{\text{cov}}^{(i)} (\hat{\mathbf{x}}_{k+1}^{(i)} - \hat{\mathbf{x}}_{k+1})(\hat{\mathbf{y}}_{k+1}^{(i)} - \hat{\mathbf{y}}_{k+1})^{\mathrm{T}} + \mathbf{R}_{k+1} \quad (24)$$

$$\mathbf{K}_{k+1} = \mathbf{P}_{xy}\mathbf{P}_{yy}^{-1} \quad (25)$$

$$\hat{\mathbf{x}}_{k+1} = \hat{\mathbf{x}}_{k+1}^{-} + \mathbf{K}_{k+1}(\mathbf{y}_{k+1} - \hat{\mathbf{y}}_{k+1}) \quad (26)$$

$$\mathbf{P}_{k+1} = \mathbf{P}_{k+1}^{-} - \mathbf{K}_{k+1}\mathbf{P}_{yy}\mathbf{K}_{k+1}^{\mathrm{T}} = \mathbf{P}_{k+1}^{-} - \mathbf{P}_{xy}(\mathbf{P}_{yy}^{-1})^{\mathbf{T}}\mathbf{P}_{xy}^{\mathrm{T}} \quad (27)$$

where E is the expectation operator, $\boldsymbol{x}_{\mathrm{k}}$ is the true state vector, $\hat{\mathbf{x}}_k^-$ is the model prediction of the state vector, $\hat{\mathbf{x}}_k$ is the state estimate vector, k is a discrete time instant variable, $\tilde{\mathbf{x}}^{(i)}$ is the sigma point vector, $\boldsymbol{P}_{\mathrm{k}}$ is the state error covariance matrix, $\boldsymbol{f}$ is a nonlinear function for transferring states to the next time instant, $\boldsymbol{h}$ is a nonlinear function for converting states to measurements, w is a weighting coefficient, N is the dimension of the state vector and λ is a scaling parameter, satisfying $\lambda=\alpha^2$ $(L+\kappa)$ - N. The parameter α, with a typical value of 10^{-3}, is a tuning factor determining the spread of the sigma points. The constant κ is a secondary tuning parameter, usually zero. The constant β affects the weight of the first error covariance term, and the choice $\beta = 2$ is optimal for normally distributed states. Cholesky decomposition should be used for the matrix square root in (16) for computational efficiency.

An iteration of the UKF algorithm proceeds as follows:

1. Initialize, (18)
2. Estimate the a priori state vector $\hat{\mathbf{x}}_{k+1}^-$ (prediction)
   a. Generate sigma points around the previous estimate, (19)
   b. Propagate the sigma points through the nonlinear functions, (20)
   c. Calculate the state mean, (21)
3. Calculate the a priori error covariance $\mathbf{P}_{k+1}^-$, (22)
4. Estimate the a posteriori state vector $\hat{\mathbf{x}}_{k+1}$
   a. Unscented transformation of predicted measurements for capturing the mean and covariance, (23)
   b. Calculate the cross-covariance between predicted states and measurements, (24)
   c. Calculate the Kalman gain, (25)
   d. Update state estimate, (26)
5. Calculate the a posteriori error covariance $\mathbf{P}_{k+1}$, (27)
6. Return to step 2

REFERENCES

[1] F. Ghassemi, S. Tafazoli, P. D. Lawrence, and K. Hashtrudi-Zaad, "An Accelerometer-Based Joint Angle Sensor for Heavy-Duty Manipulators," *Proceedings of the IEEE International Conference on Robotics and Automation*. Washington DC, May 2002, pp. 1771 - 1776.

[2] F. Ghassemi, P. Lawrence, and K. Hashtrudi-Zaad, "Design and calibration of an integration-free accelerometer-based joint-angle sensor," *IEEE Transactions on Instrumentation and Measurement*, vol. 57, no. 1, 2008.

[3] P. Cheng, F. Linnarsson, and B. Oelmann, "Joint Angular Sensor Based on Distributed Biaxial MEMS Accelerometers," *Proceedings of the 33rd Annual Conference of the IEEE Industrial Electronics Society (IECON)*, Taipei, Nov. 2007, pp. 2242 - 2247.

[4] J. Leavitt, A. Sideris, and J. E. Bobrow, "High bandwidth tilt measurement using low-cost sensors," *IEEE/ASME Transactions on Mechatronics*, vol. 11, no. 3, 2006.

[5] G. S. Maruthi, and K. Panduranga Vittal, "Electrical fault detection in three phase squirrel cage induction motor by vibration analysis using MEMS accelerometer," *Proc. of the International Conf. on Power Electronics and Drives Systems*, 2005, vol. 2, pp. 838-843.

[6] A. Albarbar, S. Mekid, A. Starr and R. Pietruszkiewicz, "Suitability of MEMS accelerometers for condition monitoring: an experimental study," *Sensors*, vol. 8, pp. 784-799, 2008.

[7] J. Nurmi, and J. Mattila, "Detection and isolation of leakage and valve faults in hydraulic systems in varying loading conditions, Part 2: Fault Detection and Isolation scheme," *Int. Journal of Fluid Power*, vol. 13, no. 1, March 2012, pp. 17-27.

[8] J. Honkakorpi, J. Vihonen and J. Mattila, "Sensor module for hydraulic boom state feedback control", Int. Journal of Fluid Power, vol. 13, no. 3, pp. 15-23, Nov. 2012.

[9] F. J. O. Corpuz, B. C. Y. Lafoteza, R. A. L. Broas, and M. Ramos, "Design and Implementation of a Closed-Loop Static Balance System for the YICAL Leg 2 Biped," *TENCON 2009 IEEE Region 10 Conference*, Jan. 2009, Singapore.

[10] M. Quigley, R. Brewer, S. P. Soundararaj, V. Pradeep, Q. Le, and A. Y. Ng, "Low-cost Accelerometers for Robotic Manipulator Perception", *IEEE/RSJ International Conference on Intelligent Robots and Systems*, Taipei, Taiwan, Oct. 2010.

[11] R. Mahony, T. Hamel, and J-M. Pflimlin, "Nonlinear complementary filters on the special orthogonal group," *IEEE Transactions on Automatic Control*, vol. 53, no. 5, pp. 1203-1218.

[12] J. Nurmi, and J. Mattila, "Detection and isolation of leakage and valve faults in hydraulic systems in varying loading conditions, Part 1: Global Sensitivity Analysis," *Int. Journal of Fluid Power*, vol. 12, no. 3, Nov. 2011, pp. 41-51.

[13] R. Isermann, *Fault-diagnosis systems, an introduction from fault detection to fault tolerance*. Springer-Verlag Berlin Heidelberg, 2006, pp. 1- 7.

[14] S. J. Julier, and J. K. Uhlmann, "A new extension of the Kalman filter to nonlinear systems," *Proc. of AeroSense, the 11th international symposium on aerospace/defence sensing, simulation and controls*, 1997, pp. 182-193.

[15] E. A. Wan, and R. van der Merwe, "The unscented Kalman filter for nonlinear estimation," *Proc. of IEEE adaptive systems signal processing, communication and control symposium*, October 2000, pp. 153–158.

[16] M. Basseville, and I. V. Nikiforov, *Detection of abrupt changes: theory and application.* Prentice-Hall, 1993, pp. 25-40.